PROCEEDINGS, 44th Workshop on Geothermal Reservoir Engineering
Stanford University, Stanford, California, February 11-13, 2019
SGP-TR-214

Toward Magnetotelluric and Microseismic Calibration of Geothermal Reservoir Models

David Dempsey, Jeremy Riffault, Alberto Ardid, Ted Bertrand and Rosalind Archer

Engineering Science, University of Auckland, Private Bag 92019, Auckland Mail Centre, Auckland 1142, New Zealand

d.dempsey@auckland.ac.nz

Keywords: Magnetotelluric, Microseismicity, Permeability Enhancement, Geothermal Reservoir Models

ABSTRACT

Reservoir models are used to understand the current state of a geothermal resource and to predict its response to future utilization. These models are usually calibrated with records of temperature, enthalpy or pressure obtained from tests, or from operation of production and injection wells. While these data provide a continuous record of the evolving reservoir state at the location of the well, less is known about conditions further from the well. One way we fill in the gaps in our understanding is through the use of geophysical methods, e.g., a magnetotelluric (MT) survey, or microearthquake (MEQ) monitoring. These provide a semi-continuous, spatial measure of some physical quantity (e.g., electrical resistivity, density of seismic events) throughout the reservoir volume. Although it will not generally be appropriate to insert this quantity directly into a reservoir simulation, conversion to some another property – say, permeability or temperature – can provide a useful constraint on the reservoir model.

Here, we develop two techniques to infer the parameters and state of a geothermal reservoir model from frequently available geophysical data. The first inverts a synthetic MT dataset under uncertainty using a Markov Chain Monte Carlo algorithm and a simplified three-layer 1D model. Constrained by lithological data from wells, the inversion provides constraint on model lithology (permeability boundaries) and temperature isotherms away from wells. The second technique using MEQ locations and densities to estimate permeability and fluid pressure properties around a stimulated well. Synthetic tests suggest the inversion is sufficiently robust to constrain the >×10 permeability enhanced region.

These geophysical inferences could serve as a qualitative constraint, for instance, by comparison of MT inferred temperatures with those output by a reservoir model. Alternatively, the inferred properties (permeability) and state (pressure, temperature) can be quantitatively incorporated in an objective function to be minimized during model calibration, thereby directly linking geophysics and reservoir models.

1. INTRODUCTION

An important part of geothermal reservoir simulation is natural state and history matching. This is where outputs of the reservoir model are compared against data and model parameters are adjusted in order to improve the match. However, during the exploration phase of a geothermal development, direct measurements of temperature or flow in wells may be scarce. Even in well-developed systems, reservoir conditions and parameters between, below or outside the area of drilled wells must be inferred. When it comes to parameters, this inference will often be carried out by the modeler, relying on expert knowledge (e.g., a geological model mapped to the simulation grid, Milicich et al., 2015) and modeling principles (e.g., parsimonious selection of the number of rock types, geostatistical techniques such as kriging). Inference of the reservoir state – pressure and temperature – are a consequence of the model solution, enforcing mass and energy balance, applying boundary and initial conditions, and aiming to match measurements in wells.

Geophysical datasets provide another source of information about parameters and conditions in a geothermal reservoir. For instance, magnetotelluric (MT) surveys are routinely used to identify the extent and thickness of low permeability, smectite clays that serve as a caprock in some systems. As smectite tends to form within a 180 to 220°C temperature range (Morrison, 1997), its identification by MT is an indirect indicator of reservoir isotherms. Dempsey et al. (2016a), using 1D analytical solutions of heat and mass transfer, developed a method to correlate MT inverted resistivity and temperature in a well and extrapolate temperatures to other parts of the reservoir. Testing the approach using synthetic reservoir models suggested a reasonable ability to extrapolate temperature up to several kilometers from a well, although performance deteriorated around geometric complexities that would be expected in a real reservoir. Ardid et al. (2018) improved on this method by introducing an effective 3-layer MT inversion that allowed estimation of the depth uncertainty of both the temperature isotherms, and the top and bottom of the clay cap. However, there remained difficulties in the handling of geometric complexity. A similar approach to integrating reservoir and geophysical data has been presented by Mellors et al. (2013, 2015).

Catalogs of microearthquakes (MEQs) are another geophysical dataset that are often available for geothermal systems with seismic monitoring networks. Unlike MT, these data generally become available during the operational phase and, even then, only after enough time has elapsed to accumulate a sufficient record of events. A notable exception are MEQs generated during well stimulation, which can occur during the development phase of an Enhanced Geothermal System (EGS) project. MEQs, when they are well-located, can reveal the presence of well-oriented faults that may serve as either conduits or compartmentalizing structures for the reservoir (Sewell et al., 2013). Evolution of microseismicity sometimes exhibits diffusive characteristics, from which it is possible to infer formation (e.g., Shapiro et al., 1997; Rivera et al., 2017) and fault permeability (Dempsey et al., 2016b). Finally, the extent of a MEQ cloud induced around a stimulated well is often taken as a proxy for an area of enhanced permeability. However, a recent inversion study by Riffault et al. (2018) has suggested that the MEQ cloud may overestimate the volume of enhanced permeability by several orders of magnitude.

The use of geophysics to calibrate geothermal reservoir model parameters (e.g., permeability, porosity, lithologic contacts) and state (e.g., pressure, temperature) is complementary to the traditional method of enforcing model-data agreement at wells or feed-zones. One attractive aspect of geophysical data is that they tend cover much larger volumes, and potentially the entire reservoir. However, the main drawback is that they tend to measure physical properties not directly relevant to reservoir modelling (electrical resistivity), and an additional inference step must be performed to obtain quantities of interest (permeability, temperature). In this paper, we describe progress on two methods of geophysics integration: MT constraints on temperature isotherms, and MEQ estimation of permeability.

2. MAGNETOTELLURIC DELINEATION OF CLAY CAP AND TEMPERATURE CONTOURS

The MT method is a passive exploration method that involves measuring time variations in natural electric and magnetic fields to determine the subsurface resistivity structure. A geothermal MT survey involves the deployment of an array of electromagnetic sensors across a region thought to overlie a geothermal field. Natural fluctuations in solar radiation and worldwide lightning activity induce magnetic fields that penetrate the crust to varying (frequency dependent) depths, inducing electric (telluric) currents in the heterogeneously resistive crust, and which in turn are detected by the surface array. Inverse modelling of the impedance – the orthogonal ratio between measured electric and magnetic fields – is used to determine how the resistivity structure of the crust varies.

During the exploration phase, it is common to use MT surveys to locate and measure the extent of shallow conductive bodies. In geothermal settings, these are often interpreted as zones of smectite clay, formed by hydrothermal alteration of silicate rocks, and therefore indicating the current or past presence of a geothermal reservoir. A secondary feature of smectite clay is that it tends to have very low permeability, and therefore acts as a capping structure to the reservoir, preventing the outflow of hot water.

In this section, we present improvements to a methodology developed by Ardid et al. (2018) for the uncertain extrapolation of temperature isotherms away from wells. The inversion is constrained using the resistivity distribution derived from MT inversion as well as prior distributions that reflect uncertainty in the depth of the clay cap based on lithological observations in wells. The methodology is based on a stochastic inversion built in Markov Chain Monte Carlo (MCMC) that focuses on shallow structures (~2 km depths) and has so far only been applied to 2D synthetic problems.

2.1 Smectite Clay, Resistivity, Permeability and Temperature

Resistivity is probably the geophysical parameter that is most relevant to geothermal exploration. Changes of this property within a geothermal system are mainly indicative of variations in physical parameters like permeability, fluid salinity, temperature, and conductivity of the rock matrix, which has potentially been hydrothermally altered. Under special conditions, these parameters combine to generate a particularly low resistivity anomaly that may have an updoming shape. Geophysical prospecting for high-temperature geothermal resources will typically search for a relatively resistive anomaly underlying the inferred clay cap.

Hydrothermal alteration mineralogy is the change in mineralogy resulting from interactions between rock and 'hot-water' that carries dissolved metals, salts and vapors. In geothermal settings, these fluids circulate along large-scale convective flow paths, through fractures, faults and porous formations. In hydrothermal systems, there is a considerable variety of minerals, with the occurrence of each dependent on conditions at the time of their formation. Clays are phyllosilicates characterized by extremely small crystalline particles of one or more members of the clay minerals group (Grim, 1968). Clay minerals are: kaolinite, smectite, illite, chlorite, sepiolite and mixed layer clays. Each clay mineral has variations in its structural organization and amount of impurities, which define subgroups of minerals within each clay. All clays present different physical and chemical properties that derive from these variations (Murray, 2000a).

Within the group of clay minerals, smectite stands out for its electric conduction capacity, which makes it highly sensitive to electrical and electromagnetic prospecting methods. In geothermal systems, a mineral subgroup of smectite called montmorillonite is usually found. Montmorillonite is formed through the alteration of silicate minerals in alkaline conditions, i.e., basic igneous rocks such as volcanic ash. This clay has been associated with formation temperature lower than 220 ºC (Browne, 1978). At higher temperatures, smectite minerals begin to alter to illite.

The amount of smectite and illite depends on temperature and permeability. Permeability and smectite temperature formation have an inverse relationship, where high permeability is related to low formation temperature, as shown by Gunerson (2000) using data from drilling. The author argued that pure smectite is found at 70ºC in conditions of high permeability and iron supply (ideal conditions). In normal permeability conditions, a mix of smectite-illite is found at a range of 150 – 200ºC and pure illite at 200-240ºC. In conditions of extremely low permeability, smectite-illite at 200-350ºC have been found Gunerson (2000, p. 1175).

2.2 Resistivity-Temperature Correlation and Extrapolating From the Borehole

In geothermal exploration, one of the primary goals is to elucidate the subsurface temperature distribution, usually investigated by direct measurements in wellbores. However, it is difficult to infer how temperature varies away from the borehole. Ardid et al. (2018), as an extension of Dempsey et al. (2016b) presented a new approach for the uncertain estimation of isotherms and clay cap boundaries in a geothermal field, using the temperature log from one well and the electrical resistivity derived from MT inversions. Their methodology focused on the relationship between temperature and resistivity assuming a correlation between the shallow (clay) resistivity anomaly and clay formation temperatures.

The principle advantage of our approach is the explicit investigation and visualization of inversion uncertainty, yielding inferred depth intervals for clay cap boundaries and temperature isotherms for the upper 2 km. Our stochastic inversion is based on MCMC fitting of a one-dimensional 3-layer resistivity model beneath each MT station, where the middle layer is assumed to represent the conductive clay

cap. A temperature profile is derived for each 3-layer model by fitting a piecewise 1D solution for mixed conductive-advective heat transfer (Bredehoeft and Papadopulos, 1965; Ardid et al., 2018)

$$T' = \frac{\exp(\beta z'/L) - 1}{\exp(\beta) - 1}, \quad z' = \frac{z - z_{\min}}{z_{\max} - z_{\min}}, \quad T' = \frac{T - T_{\min}}{T_{\max} - T_{\min}} \tag{1}$$

where T_{min} and T_{max} are values of temperature at the layer boundaries z_{min} and z_{max}, and the transport values β_i are fitted to the measured wellbore temperature profile in each layer and then carried across to the inferred 3-layer model. The resulting inversion is able to recover some general features of a synthetic temperature distribution generated by a reservoir simulator. However, it is necessary to extend the study to consider more than one well, thus approaching a more realistic field case where more information is usually available. In future, we intend to assess the efficacy of this approach through application to a well-characterized field site.

2.3 Using Information From More than One Well to Constrain Inversion

This section presents an extension of the Ardid et al. (2018) methodology in which lithology information from more than one well are used to constrain the MT inversion. This is carried out through the inclusion of priors for boundaries of the 3-layer model MCMC inversion. The prior is varied to capture the spatial dependence of parameter uncertainty between stations and wells. Our results indicate that the approach improves the estimation of clay cap boundaries and the extrapolation of temperatures, while still providing reasonable constraints on the uncertainty of these estimates.

2.3.1 Methodology

For each station, a 1D 3-layer resistivity profile is estimated where the locations of interfaces (clay cap boundaries) and resistivity are considered unknown quantities. It is assumed that their values are independent in the vertical direction and dependent in the horizontal direction, where the dependency is model as a Gaussian prior.

For each MT station, let $\hat{\boldsymbol{\rho}}_{app}$ represent the MT data (apparent resistivity) across all frequencies, $\mathbf{z}$ represents the unknown depths of layer boundaries, and $\boldsymbol{\rho}$ the unknown layer resistivities. The Bayesian model that defines a joint posterior probability distribution function of all unknown parameters is:

$$f(\boldsymbol{\rho}, \mathbf{z} \mid \hat{\boldsymbol{\rho}}_{app}) \propto f(\hat{\boldsymbol{\rho}}_{app} \mid \boldsymbol{\rho}, \mathbf{z}) \prod_{i=1}^{N_{layers}} f(\rho_i) \prod_{j=1}^{N_{boundaries}} f(z_j) \tag{2}$$

The first factor on the right defines the likelihood function which relates the unknown parameters and the MT data. The likelihood function for MT data is given by the misfit between the data and the corresponding simulation results assuming normally distributed errors. Let ε_{pi} be the misfit between the data and simulation for period, p, and station, i. Then the likelihood function is given:

$$f(\hat{\boldsymbol{\rho}}_{app} \mid \boldsymbol{\rho}, \mathbf{z}) \propto \prod_{p=1}^{N_{periods}} \prod_{i=1}^{N_{stations}} \exp\left(-\frac{\varepsilon_{pi}^2}{2\sigma^2}\right) \tag{3}$$

where σ^2 is the measurement error.

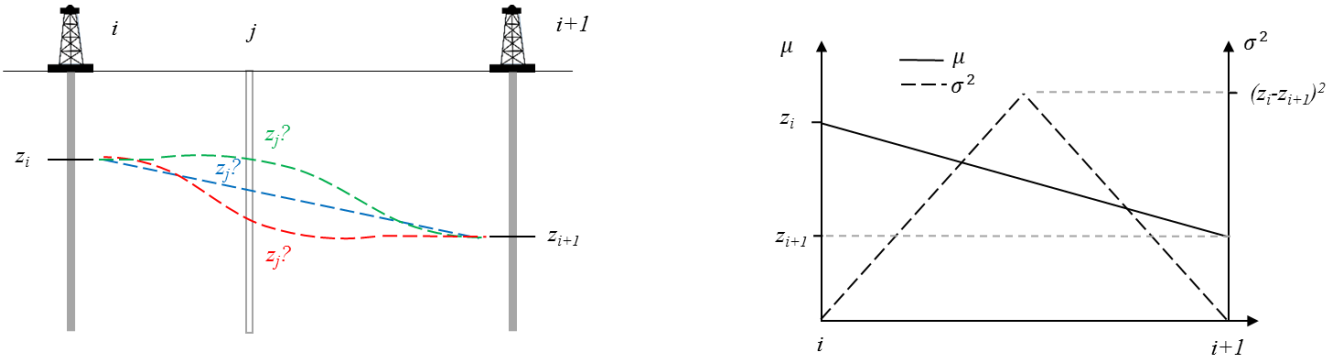

Figure 1: Uncertain inversion for layer position at *j* between known depths at *i* and *i+1*. (left) Blue, red and green dashed lines show possible interface positions. (right) Mean (solid) and variance (dashed) of prior distribution for inversion at *j* between *i* and *i+1*.

The second and third factors on the right of (2) are prior probability distributions for resistivity and depth, respectively. We use these to incorporate other information as a constraint on the inversion. If lithology information in wells is available then layer boundary parameters can be fixed at these locations (Figure 1). Between two adjacent wells, where layer positions are unknown and must be determined by inversion, we can still draw on constraint from the known lithology to specify a normally distributed prior, $\mathcal{N}(\mu,\sigma^2)$, with mean μ and variance σ^2. Suppose that z_i and z_{i+1} are the known positions of a layer boundary in wells i and $i+1$. Then, our best prior estimate, μ, of the layer boundary at the location j between i and $i+1$ is the straight line adjoining z_i and z_{i+1} evaluated at j. We further assume that the uncertainty, σ^2, reaches a maximum of $(z_i - z_{i+1})^2$ equidistant between i and $i+1$, decreasing linearly to 0 at the two wells. Thus, for inversion closer to a well, μ will be more similar to the true parameter values in the well and σ will decrease to zero (certainty of the true value).

2.3.2 Constrained Inversion Results

We apply our constrained inversion to the synthetic problem presented in Ardid et al. (2018). Figure 2 presents uncertain estimation of the top and bottom boundaries of the clay cap using the synthetic model detailed in Ardid et al. (2018) and an inversion algorithm modified with improved priors. Figure 3 presents the extrapolated isotherms. Recovery of the layer boundaries and isotherms is improved compared to the inversion without priors.

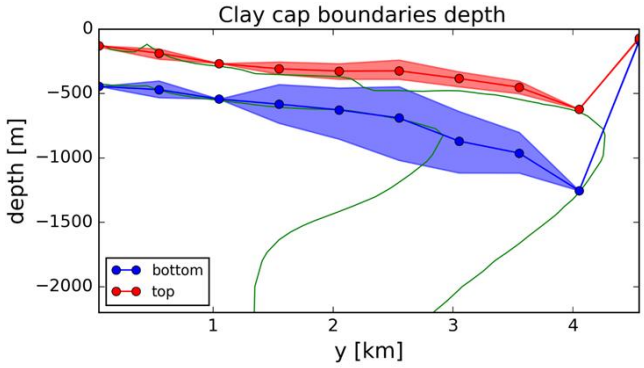

Figure 2: Inversion for the top (red) and bottom (blue) of the conductive clay cap (green lines) obtained from a synthetic reservoir model. The shaded envelope at each horizontal location gives the [5, 95] percentile uncertainty on depth. Wells are assumed to provide information for the inversion at *y* = 0, 1 and 4 km, and hence the uncertainty at these locations is zero.

From Figure 2, it is clear that uncertainty reduces towards the wells, as expected. Due to the diffusive nature of penetrating electric fields, MT inversions tend to have less resolution with depth, and this is reflected in the higher degree of uncertainty in determination of the bottom boundary of the clay cap compared to the top. On the other hand, an encouraging result is that the inversion identifies the absence of the clay cap at the station located at y = 4.5 km, which could be useful for estimating the extent of a geothermal resource. Although our inversion is unable to capture the change in geometry of the clay cap, from predominantly horizontal at the origin rotating to a vertical orientation at 3 km, the elevated uncertainty in the vertical section somewhat encapsulates this model inadequacy

Figure 3 shows the uncertain temperature extrapolation compared against the known values from the synthetic model. Isotherm envelopes are constructed from 500 samples recovered from the MCMC inversion, plotting 5%-95% percentile depths for each isotherm value. Extrapolation recovers major aspects of the geometric behavior, including the approximate depths and deepening trend with distance from the upflow. Compared to previous approaches (Dempsey et al., 2016; Ardid et al., 2018), this inversion has two desirable aspects: first, the extrapolation captures inversion of the 180ºC and 220ºC isotherms at around 3 km, assigning greater uncertainty in this section. Second, extrapolation captures the termination of these isotherms and thus provides a measure of resource extent.

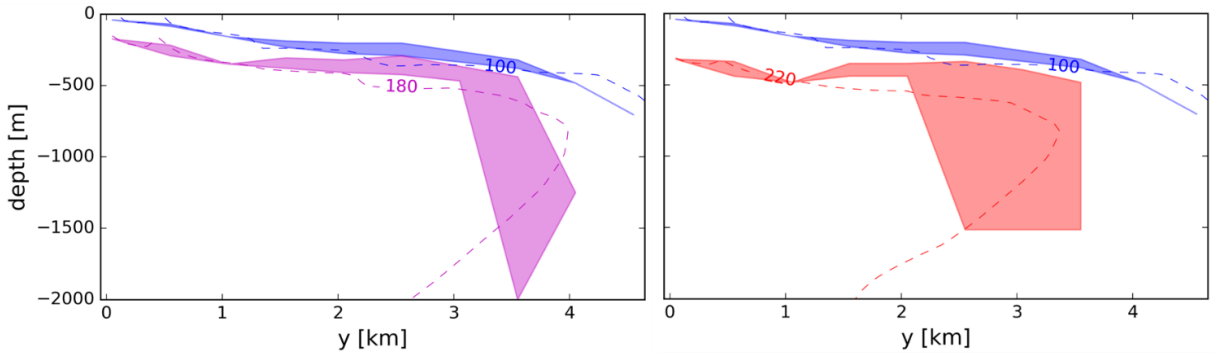

Figure 3: Uncertain inversion for the 100ºC (blue), 180ºC (left, purple) and 220ºC (right, red) isotherms. Shaded envelopes at each horizontal location gives the [5, 95] percentile uncertainty on depth. The true value from the synthetic model is given by the dashed lines.

By introducing lithological data from wells as a prior constraint on our inversion, we have improved the recovery of the clay cap geometry and temperature isotherms. However, there remain several areas for improvement and extension. For instance, it would be worthwhile exploring how different misfit formulations, ε_{pi}, might affect recovery of complementary aspects of the shape and magnitudes of the low resistivity anomaly. Currently, we fit the apparent resistivity and phase of the TE and TM mode; however, fitting other parts of the impedance tensor, like the determinant or other rotational invariants, could change the inversion. Finally, the efficacy of this inversion method can only be assessed by application to a well-characterized field site.

3. MICROSEISMIC DELINEATION OF PRESSURE INCREASE AND PERMEABILITY ENHANCEMENT

The rate of earthquakes occurring in geothermal fields is often higher than the regional average, or the rate in the field prior to development. This indicates that some fraction – probably most – of these events, are being directly triggered by operational activities like brine reinjection (e.g., Sewell et al., 2013), production (Brodsky and Lajoie, 2013) or well stimulation (e.g., Benato et al., 2016). In most cases, induced earthquakes are triggered by a local increase of the pore fluid pressure that reduces the effective normal stress across fracture planes, however poroelastic and production-related mechanisms have also been suggested (e.g., Segall and Lu, 2015). Interpreting earthquake triggering in terms of fluid pressure increase provides a route to inferring fluid pressure changes, and the permeability structures controlling these, across different parts of a geothermal field.

Riffault et al. (2018) presented a method that uses a MEQ cloud to invert for permeability changes around an EGS well during high pressure injection. The method involves first computing a probabilistic hypocenter density, n, for the stimulation, defined as the number of events per unit volume (Dempsey et al., 2016c), taking account of location (epistemic) and Poisson triggering (aleatoric) uncertainty. This quantity, a function of radial distance, r, and time, t, is assumed to depend linearly on the pressure increase, i.e., $n(r,t)=k(\Delta P(r,t)-\Delta P_{crit})$, where k and ΔP_{crit} are the unknown proportionality factor and critical pressure increase. Then, a library of parameterized permeability enhancement scenarios, $\kappa(r,t:\boldsymbol{\theta})$, are implemented within a reservoir simulator, where $\boldsymbol{\theta}$ is a vector of parameters. The injection phase is simulated for different combinations of $\boldsymbol{\theta}$, k and ΔP_{crit}, until a good match is obtained between the modelled and observed hypocenter density. Applying this method to the EGS stimulation at Paralana in South Australia, they showed that permeability enhancement only occurred within a 30 m radius from the borehole, whereas the MEQ cloud extended up to 400 m away. The immediate implication is that MEQ clouds are a poor indicator of stimulated reservoir volume. In this section, we extend the inversion method of Riffault et al. (2018) from a 1D radial geometry to 2D planar, targeting in particular the azimuthal heterogeneity often observed in the MEQ cloud.

3.1 Induced Earthquake Hypocenter Density

In Riffault et al. (2018), hypocenter density was computed by integrating probability density functions (PDF) representing the location of each event – a multivariate normal distribution – over concentric shells centered on the wellbore. In the two-dimensional case considered here, we now have to integrate the location PDF over rectangular boxes instead of annuli. An event is defined by its position, $[x_i, y_i, z_i]$, and horizontal and vertical uncertainties σ_{xy} and σ_z, respectively. A volume is defined by a system of six coordinates, $[X_1, X_2, Y_1, Y_2, Z_1, Z_2]$. The probability, p_{si}, that an event, i occurred within the volume, s is $p_{si} = p_{xi}(X_1,X_2) \times p_{yi}(Y_1,Y_2) \times p_{zi}(Z_1,Z_2)$, where $p_{ji}(J_1,J_2)$ is the integral of the normal distribution $\mathcal{N}(j_i, \sigma_j)$ over the limits $[J_1,J_2]$. As in to Riffault et al. (2018), summing over all events in the catatlog yields a Poisson binomial distribution, approximated as a discretized normal distribution of mean $\mu_{locs} = \sum p_{si}$ and variance $\sigma^2_{locs} = \sum (1- p_{si})p_{si}$ for each volume, s. This is converted to a hypocenter density, $n(\mathbf{x},t)$, by dividing by the volume area, $S = (X_2 - X_1)(Y_2 - Y_1)$.

One difficulty interpreting earthquake observations is the inherent randomness embedded in a Poisson triggering process. If, in a given week, two earthquakes are observed to occur in a particular volume, then the most-likely rate parameter – the quantity we are comparing with models of fluid pressure – for the Poisson process is 2 events per week. However, it is also possible (but less likely) that the rate parameter is 1.8 events per week, or 2.3, or indeed 102.3 (very unlikely). From an inference perspective, the rate parameter is itself a Poisson probability distribution with mean given by the observed value. Riffault et al. (2018) account for this additional layer of uncertainty by summing over Poisson distributions with different possible rate parameters, which has the effect of widening the PDF for $n(\mathbf{x},t)$.

3.2 Two-Dimensional Flow Models with Permeability Enhancement

To invert for pressure and permeability changes from MEQ data, we require a forward model that utilizes these components, either as inputs or intermediate quantities. Following Riffault et al. (2018), we assume a simple linear model relating pressure increase and hypocenter density, $n(\mathbf{x},t)=k(\Delta P(\mathbf{x},t)-\Delta P_{crit})$. The pressure increase $\Delta P(\mathbf{x},t)$ is obtained from the nonisothermal reservoir flow simulator FEHM (Zyvoloski, 2007), coupled to a wellbore simulator that accounts for heating effects during injection. FEHM has been modified to accept an arbitrary permeability evolution model, $\kappa(\mathbf{x},t:\boldsymbol{\theta})$, which provides the necessary link between MEQs (n) and the quantities for inference (ΔP, κ).

3.2.1 Permeability model

As our goal is to model a high degree of permeability heterogeneity we require a lot of flexibility (parameters) in $\kappa(\mathbf{x},t:\boldsymbol{\theta})$ such that each model block can exhibit a degree of independence from its neighbors. As there are an infinite number of permeability evolution scenarios, we introduce several constraints:

(i) Permeability enhancement should be highest close to the well and decrease with distance.

(ii) Permeability enhancement cannot occur in volumes which have not recorded seismic activity. This is because we have no information here from which to derive permeability. A drawback of this constraint is that it neglects the possibility of aseismic slip and permeability enhancement.

(iii) Permeability enhancement is irreversible. This may not be always be the case, especially if elastic opening is involved in the real stimulation processes

These three constraints encode modeler insight, discarding permeability enhancement scenarios deemed unrealistic and in the process simplifying the inversion process by narrowing the range of possible permeability enhancement scenarios. Additionally, a design decision to consider is the trade-off between flexibility and reduction of parameter space complexity. The 2D inversion introduces more flexibility than the radial version, but this comes with a higher computational burden.

Isotropic permeability, $\kappa_i(t)$, evolution with time, t, is set according to a logistic function, different in each model block, i. This function is governed by five parameters (Figure 4). (i) Initial permeability, $\kappa_{0,i}$, sets the lower asymptote. (ii) Permeability change, $d\kappa_i$, gives the difference between lower and higher asymptotes in log(m^2). (iii) Timing of permeability change, $t_{1,i}$, is the time at which $\kappa_i(t) = \kappa_{0,i} + d\kappa_i/2$. (iv) Permeability change characteristic time, $t_{2,i}$, controls the ramp width of the logistic function. (v) Geometry value, b_i, controls the geometry of the logistic function. For $b_i = 0$, the logistic function is symmetric about $t_{1,i}$. For $b_i < 0$ the logistic function has a steeper early increase and a smoother increase to its upper asymptote, and vice versa for $b_i > 0$. A ranking system is used in the assignment of values $\kappa_{0,i}$, $d\kappa_i$, $t_{1,i}$, $t_{2,i}$, and b_i to enforce constraint (i) above, that enhanced permeability should decrease with greater distance from the well.

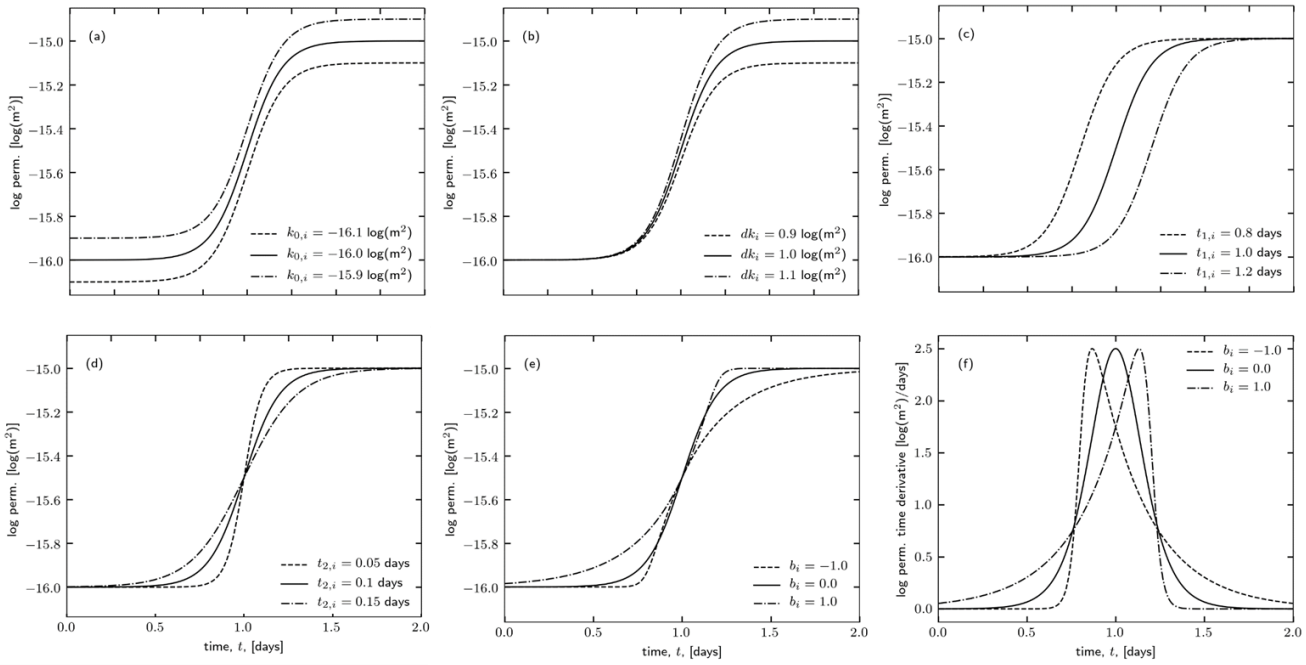

Figure 4: Model block permeability enhancement functions. Variability with (a) initial permeability, (b) permeability increase, (c) stimulation time, (d) stimulation length, (e-f) geometry factor.

This permeability model has hundreds of free parameters compared with the nine parameter radial model used by Riffault et al. (2018). It also introduces an element of bias to the inversion, with the obvious sources being our constraints (i), (ii), and (iii). Averaging of permeability over large volumes may also affect the inversion results and recovered permeability distribution. Finally, the logistic function, while flexible, is not able to reproduce all scenarios, such as, say, a two stepped permeability increase. Nevertheless, addressing these biases would require an even larger number of parameters, and the inversion may simply become impossible. The introduction of bias is inherent and inescapable when managing the trade-off between model simplicity and flexibility.

3.2.2. Synthetic forward flow model

As for radial inversion in Riffault et al. (2018), we use the groundwater flow simulator FEHM to solve for ΔP as a function of $\mathbf{x}$, t, and a given a permeability enhancement scenario over N model blocks, $\boldsymbol{\theta} = [\ \kappa_{0,1}, d\kappa_1, t_{1,1}, t_{2,1}, b_{1,\ \ldots}\ \kappa_{0,N}, d\kappa_N, t_{1,N}, t_{2,N}, b_N]$. Extension to a two-dimensional geometry necessitates a considerably coarser grid than for the radial case in order to limit computation times and parameter space. Similarly, time steps must be longer, which means that both space and time discretization potentially influence the simulated pressure and, hence, the inverted parameters.

To test our inversion, we set up a synthetic forward model using a "known" permeability enhancement scenario $\boldsymbol{\theta}$. We then simulate $\Delta P(\mathbf{x},t)$ around a well under a fixed injection rate, convert this to a triggering rate $n(\mathbf{x},t)$, and then generate N_e earthquake observations with positions, $\mathbf{x}_i$, and times, t_i, using a Poisson sampler. Zero heat and mass flow boundary conditions are enforced at all boundaries, and pressure changes are checked that they remain negligible here. Unlike Riffault et al., (2018), porosity is kept constant and does not depend on permeability, as the instabilities this relation can introduce considerably slow the average model running time. Model parameters are reported in Table 1 and the synthetic model is summarized in Figure 5.

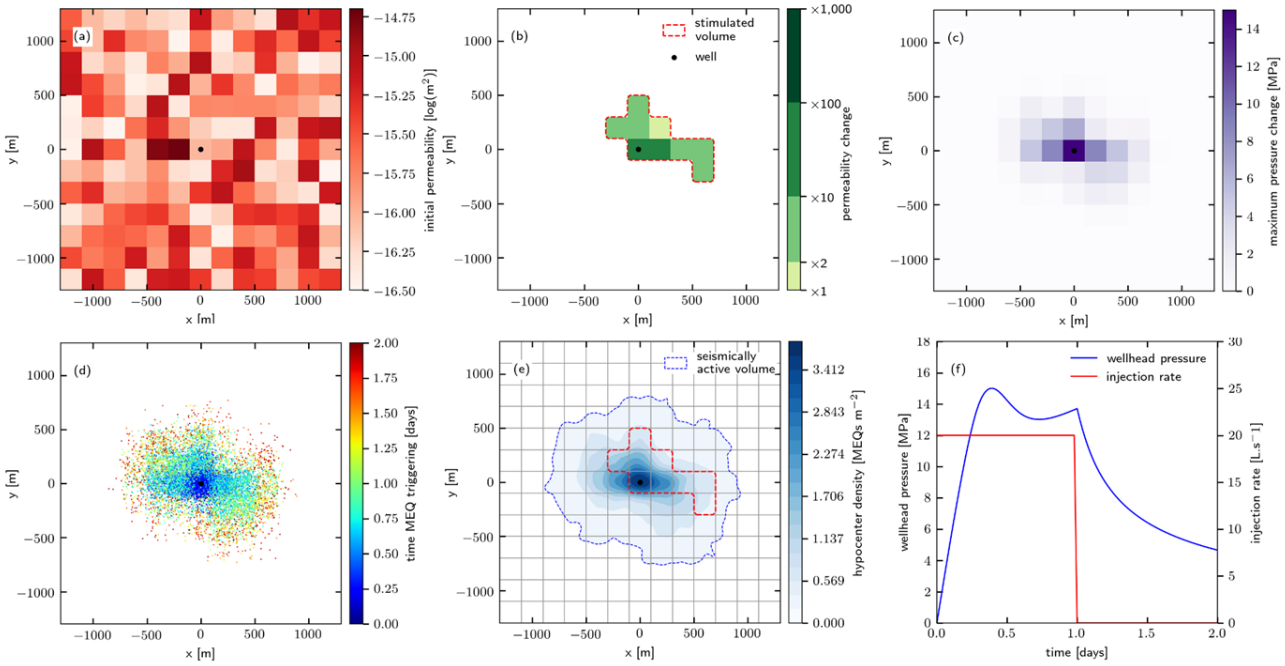

Figure 5: Summary of synthetic forward model. (a) Initial permeability distribution, (b) final permeability enhancement, (c) maximum fluid pressure during injection, (d) distribution of MEQs, (e) contours of computed hypocenter density, and (f) simulated wellhead pressure during and after injection. The goal of inversion is to use the MEQs (d) and wellhead pressure record (f) to recover permeability (a) and enhancement (b).

Simulated downhole pressure is assumed to be recorded and later used for the inversion process. The most severe effect of the coarse mesh discretization is on the wellbore pressure calculation. In Riffault et al. (2018), blocks near the wellbore were set a radial thickness of only 0.2 m to avoid interference with calculations. Here, the well is at the center of a rectangular volume of dimension 200×200×20 m^3. The calculated average pressure of this block may be significantly different from the downhole pressure. Approximations exist to obtain equivalent pressures, using the analytical solution of radial flow within one block (Peaceman, 1978), but they only apply to steady state and constant permeability situations, and therefore are not applicable here. Another option is to increase mesh resolution closer to the well, but to do so would introduce asymmetries that may bias the permeability inversion process later on. The best thing we can do is to not consider calculated pressure in the initial stages of the simulation, when injection at constant flow rate is filling the well block and its size will affect calculated pressure the most. Following this phase, pressure should be more stable and, in attempting to replicate the synthetic wellbore record, discretization effects will be less severe. To determine how long this stage lasts, we use the diffusion characteristic time, t_{diff}, derived by Shapiro et al. (1997), $t_{diff} = x^2_{block}/(4\,\pi^2\,D)$ where x_{block} is the model block size and the diffusivity, D, is given $D = \kappa_{0,w}/(\mu\,(\phi\,c_f + c_r))$, where $\kappa_{0,w}$ is the initial permeability at the well, μ is viscosity, ϕ is porosity, and c_f and c_r are respectively the fluid and rock compressibility.

3.3 Permeability Inversion

The goal of computational inversion is to determine the values of a model's parameters that minimize its misfit with available data. When the parameter space has a high dimension, it is preferable to hand inversion off to an algorithm specialized in exploration and exploitation (finding the minimum). These methods typically rely on some quantified measure of model misfit, as well a range of parameters controlling algorithm behavior.

3.3.1 Objective Function for Determining Model Fitness

Our synthetic inversion problem is constrained by the MEQ cloud and the borehole pressure record. Misfit against both these quantities is balanced in a combined objective function, $S(\theta)$,

$$S(\theta) = -\sum_{i=0}^{N_f} \frac{1}{\sigma_P^2}(\bar{P}_i - P_i(\theta))^2 - w\sum_{j=0}^{N_{blocks}} \frac{1}{\sigma_j^2}(\bar{n}_j - n_j(\theta))^2 \qquad (4)$$

where w controls the tradeoff between wellhead pressure and seismicity, P_i and n_j simulated wellbore pressure and hypocenter density, overbarred quantities are corresponding observations, and σ are the observation errors.

3.3.2 Genetic Algorithm for Exploring Parameter Space

For the nine parameter forward model used by Riffault et al. (2018), inversion was undertaken using a MCMC algorithm that also output posterior parameter distributions. MCMC algorithms scale poorly with the dimensionality of parameter space and it was therefore necessary to consider alternative calibration techniques for the 2D inversions. Here we explore the use of a genetic algorithm.

We use the following definitions. A population of individuals, each defined by its genotype, $\boldsymbol{\theta}$, is evolved toward a better solution, in the sense that their fitness, $S(\boldsymbol{\theta})$, is increased. At each iteration (a new generation), we evolve the population, keeping the population size, N_{pop}, constant. There are four steps to evolve from one generation to the next:

(i) Fitness selections – individuals with fitness too low are eliminated. We do this by randomly selecting three individuals and keeping only the fittest. This is repeated until we recover N_{pop} individuals. This means that some individuals are present multiple times in our population. To avoid converging to a local minimum, we added an anti-crowding feature: the 10% best fitnesses are assigned the same maximum value for the ranking process.

(ii) Crossover – mixing of the population genotypes. This keeps the overall population genotype consistent and avoids different individuals drifting separately to different fitness maxima. We do this by dividing the population into couples, where each couple has the probability P_{cross} to be replaced by its two offspring, which are the complementary randomly mixed genotypes of the parents.

(iii) Mutation. This is the step that controls parameter space exploration. Each individual in the population has the probability P_{mut} to undergo mutation. If it does, each of its parameters (or genes), ω, has the probability $p_{mut,\omega}$ to be transformed to $\omega = \omega + \mathcal{N}(0, \sigma_{mut})$, where σ_{mut} is the mutation rate.

(iv) Compute fitness of new individuals: The forward model is run and $S(\boldsymbol{\theta})$ calculated for each new individual generated through crossover or mutation.

The final step is the most computationally expensive but it is also massively parallelizable as, within a generation, each individual fitness is independent. The first generation requires N_{pop} forward runs and each subsequent generation requires on average $N_{pop} \times [1 - (1 - P_{cross})(1 - P_{mut})]$ new individuals. For the parameters listed in Table 1, this is approximately 260,040 forward runs. We use 7 cores, and a forward run takes about 15 seconds to complete, thus the typical inversion process lasts about one week.

Table 1: List of parameters for synthetic model inversion.

Flow model parameter	*Value*	*Inversion parameter*	*Value*
Initial pressure [MPa]	47	Objective function weight, w	10^3
Initial temperature [°C]	250	Population size, N_{pop}	500
Thermal cond. [Wm^{-1} K^{-1}]	2.2	Number of generations, N_{gen}	1000
Density [kg m^{-3}]	2681	Crossover probability, P_{cross}	0.4
Specific heat [kJ m^{-3} K^{-1}]	2.0	Mutation probability, P_{mut}	0.2
Vertical thickness [m]	40	Individual parameter mutation probability, $p_{mut,\omega}$	0.05
Spatial discretization [m]	200	Mutation rate, σ_{mut}	0.02
Model horizontal extent [m]	[-1200, 1200]	Fitness threshold, S_{thres}	$2\times S(\boldsymbol{\theta}^*)$
Seismicity proportionality, k [events km^{-2} MPa^{-1}]	2000		
Critical pressure, ΔP_{crit} [MPa]	0.05		
Catalog size, N_e	10007		
Horizontal location error, σ_{xy} [m]	84		
Porosity [%]	2		

Indeed, due to observation errors, if we suppose the existence of a "true" parameter vector $\boldsymbol{\theta}_{true}$, this will not necessarily be the same parameter set $\boldsymbol{\theta}^*$ that minimizes, $S(\boldsymbol{\theta})$. Thus our inversion should focus on the bounding of $[\boldsymbol{\theta}_{true}]$. Unfortunately, a genetic algorithm does not return a posterior distribution as a MCMC does. As an alternative, we chose to select all the parameter sets with fitness higher than a threshold, S_{thres}. This ensemble, $[\boldsymbol{\theta}]_{Sthres}$, is assumed to have a reasonable chance to contain $\boldsymbol{\theta}_{true}$. The choice of threshold is arbitrary and a potential issue. Setting the value too high may exclude the true parameters while setting it too low might give unreasonably large parameter ranges that offer no significant constraint.

The inversion depends on several parameters that must be set arbitrarily, assisted by the experience of the modeler: the genetic algorithm parameters, $[N_{pop}, N_{gen}, P_{cross}, P_{mut}, p_{mut,\omega}, \sigma_{mut}]$, the objective function weight, w, and the fitness threshold, S_{thres}. The values we have used are listed in Table 1, although some were adapted, sometimes during an inversion, as insight was gained as to how each altered efficiency and success. A parameter set might be useful for a first fast narrowing of the parameter space but inefficient for later refinements: typically the mutation rate, σ_{mut}, should be lowered as the maximum fitness is approached. A parameter set may also be efficient for one problem but ill-adapted for another.

3.3.3 Inversion Results and Limitations

Applying the inversion described above, we obtain the results in Figures 6 and 7. In general, the best inverted model does a reasonable job capturing the asymmetry in permeability enhancement about the borehole reflected in the true model. The magnitude of permeability enhancement is also reasonably well captured, although only at an order-of-magnitude accuracy. One, albeit imperfect, way to visualize

uncertainty in the solution is to show the maximum and minimum permeability enhancements at each grid block across all "acceptable" models, $S > S_{thres}$. These suggest a reasonable degree of uncertainty in the extent of the modestly stimulated reservoir (>×2 permeability enhancement), but consistent agreement on the extent of the robustly stimulated region (>×10). Initial permeability is reasonably well determined within the area of the MEQ cloud, but is poorly constrained outside this region.

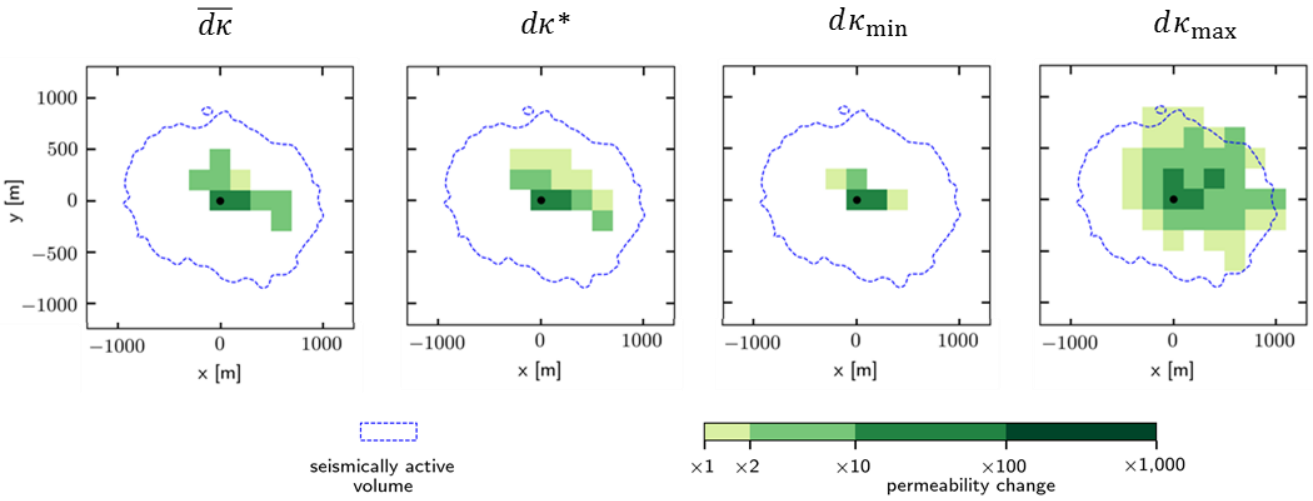

Figure 6: Results from synthetic inversion of permeability enhancement. From left to right: true permeability enhancement, best inversion, minimum enhancement of all acceptable models, maximum enhancement of all acceptable models, $S > S_{thre}$.

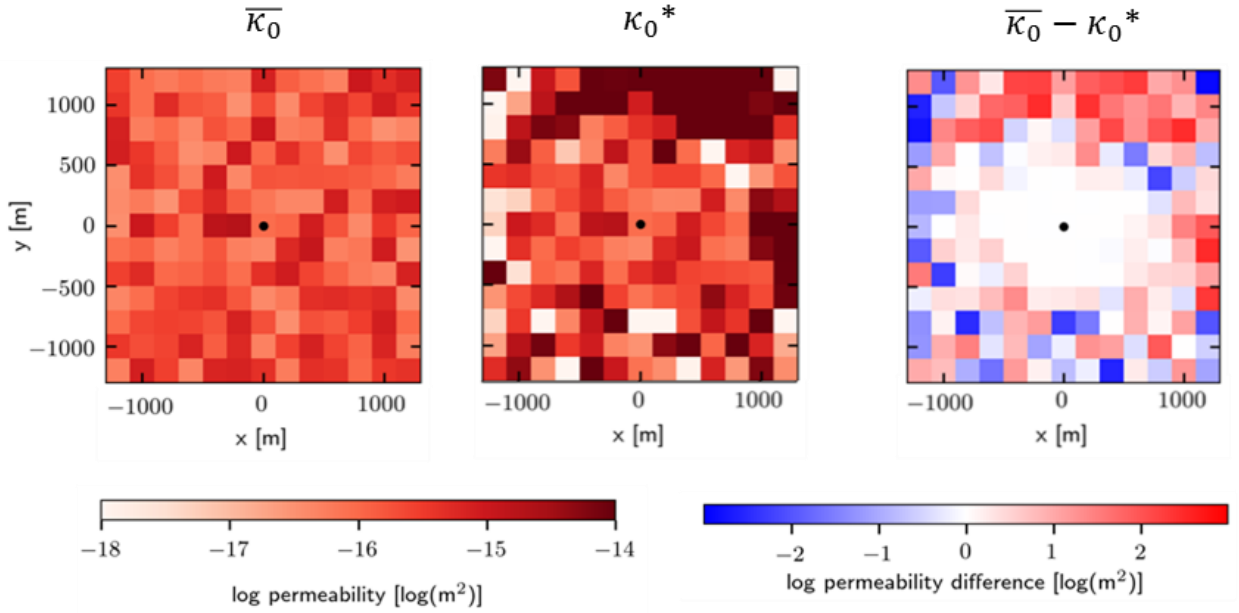

Figure 7: Results from synthetic inversion of initial permeability. From left to right: true initial permeability, best inversion, residual.

We have rerun the inversion using a smaller location error of a catalog with 10× fewer events and obtained similar inversions for permeability enhancement. We also recover intervals that successfully bracket the true value of porosity and the seismicity parameters k, and ΔP_{crit}, although the latter is several orders-of-magnitude wide, providing poor constraint.

We have investigated the impact of space and time discretization on our inversion method. We do this by rerunning forward models to generate synthetic datasets at fine resolution in either time or space, and then attempting to recover the "known" permeability enhancement using a coarse resolution model for inversion (Figure 8). The results are qualitatively similar to those shown in Figure 6, that is, the spatial extent and magnitude of the robustly stimulated region (>×100) is somewhat well captured, but performance deteriorates when trying to image the modestly stimulated reservoir. There is clearly more work to be done in improving the inversion technique.

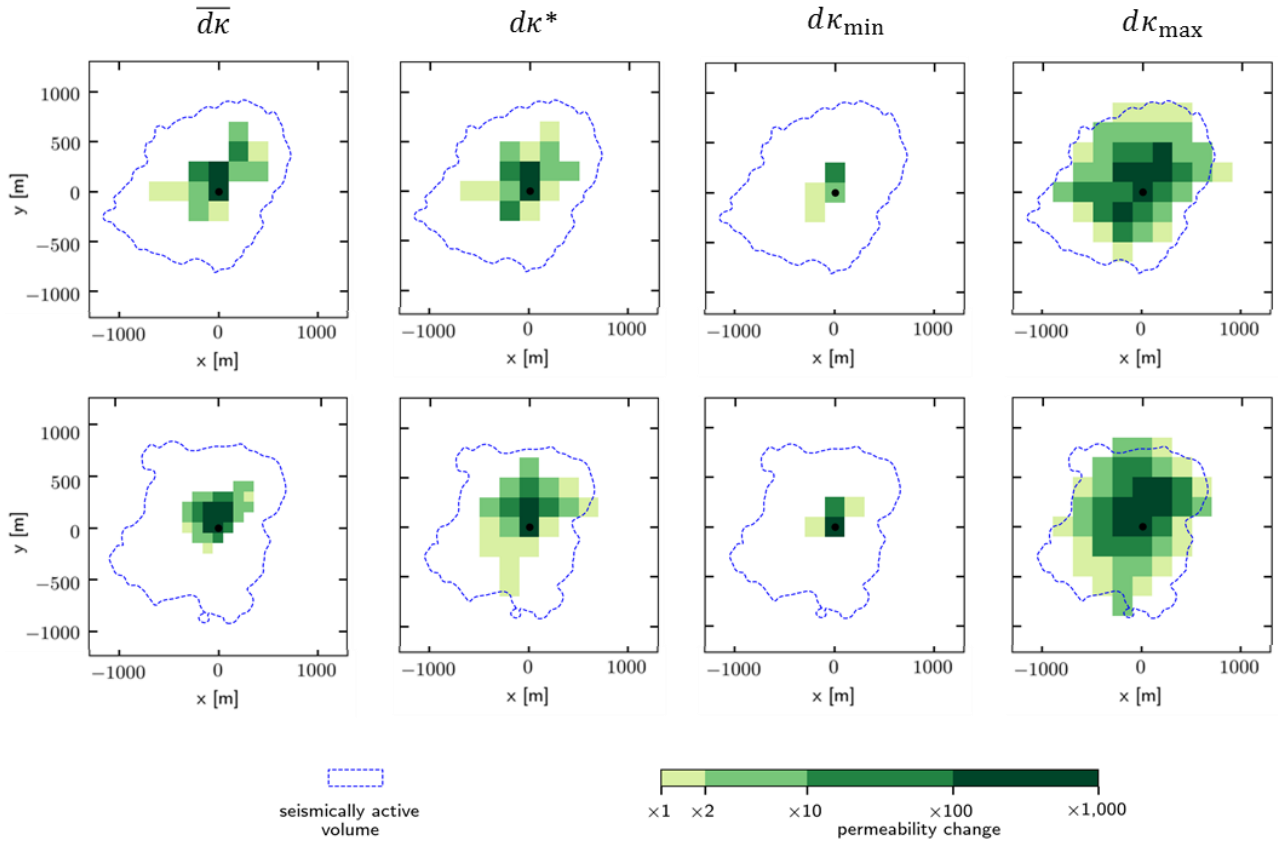

Figure 8: Synthetic inversions using a 2x coarser time step resolution (top row) and a 2x coarser spatial resolution (bottom). From left to right: true permeability enhancement, best inversion, minimum enhancement of all acceptable models, maximum enhancement of all acceptable models, $S > S_{thre}$.

4. TOWARD GEOPHYSICAL CALIBRATION OF RESERVOIR MODELS

For convenience, we can define spatiotemporal outputs of the reservoir model, pressure and temperature - $P(\mathbf{x},t;\boldsymbol{\Theta})$ and $T(\mathbf{x},t;\boldsymbol{\Theta})$, in terms of the model input parameters, $\boldsymbol{\Theta}$. Input parameters commonly include permeability and porosity of individual model blocks, deliverability parameters of feedzones, and mass or heat sources at the model boundaries. Calibration of the reservoir model is the process of minimizing the model misfit to the wellbore data, $S_0(\boldsymbol{\Theta})$, through modifications to $\boldsymbol{\Theta}$, i.e.,

$$S_0(\Theta) = -w_{P,WB}\sum(\overline{P}_{WB,i} - P_{WB,i}(\Theta))^2 - w_{T,WB}\sum(\overline{T}_{WB,i} - T_{WB,i}(\Theta))^2 \qquad (5)$$

where $w_{P,WB}$ and $w_{T,WB}$ balance the misfit between wellbore observations of pressure and temperature (this could be generalized to include quantities derived from P and T, e.g., wellbore flows, enthalpies, etc.)

The work presented in Sections 2 and 3 are part of a larger research direction exploring the use of geophysical datasets as quantitative constraints during reservoir model calibration (Figure 9). Thus, we need a way to quantitatively incorporate the insights obtained from the MT and MEQ inversions into the model misfit, $S_{gp}(\boldsymbol{\Theta})$. For contours of inferred temperature (Section 2) or pressure (Section 3), these could be incorporated by a simple extension of Eq. (5)

$$S_{gp}(\Theta) = S_0(\Theta) - w_{P,MEQ}\sum(\overline{P}_{MEQ,i} - P_{MEQ,i}(\Theta))^2 - w_{T,MT}\sum\frac{1}{\sigma_i^2(\mathbf{x})}(\overline{T}_{MT,i} - T_{MT,i}(\Theta))^2 \qquad (6)$$

where pressure observations are now a mix of direct wellbore, P_{WB}, and inferred MEQ, P_{MEQ}, and temperature observations include wellbore, T_{WB}, and MT inferred temperature contours, T_{MT}. The degree to which fitting the different observations or inferences are prioritized depends on the relative magnitude of the weighting terms, $w_{P,WB}$, $w_{P,MEQ}$, $w_{T,WB}$ and $w_{T,MT}$. The term, σ_i^2, weights misfit with the inferred MT isotherms in terms of the degree to which the 1D three-layer MT inversion at $\mathbf{x}$ is appropriate to the dimensionality of the MT data at $\mathbf{x}$. The different geophysical inferences will also be relevant during different model calibration phases. For instance, temperature isotherms inferred from MT can constrain the natural state model, whereas pressure changes inferred from MEQs could only be used during history-matching.

Finally, where the output of the geophysics inversion is an inference about the flow properties of the rock, then the misfit can be further modified to include a Tihkonov regularization term that penalizes parameters as they deviate from the inferred values

$$S'_{gp}(\Theta) = S_{gp}(\Theta) - w_{\theta,MEQ}\sum(\bar{\Theta}_{MEQ,i} - \Theta_{MEQ,i})^2 - w_{\theta,MT}\sum(\bar{\Theta}_{MT,i} - \Theta_{MT,i})^2 \quad (7)$$

where $\boldsymbol{\Theta}_{\mathrm{MEQ}}$ includes initial permeability and permeability enhancement parameters within the MEQ cloud, defined in Section 3.2.1, and $\boldsymbol{\Theta}_{\mathrm{MT}}$ parameterizes the depth and horizontal extent of the low permeability clay cap. As before, $w_{\theta,MEQ}$, $w_{\theta,MT}$, weight the strength of these constraints relative to the other observations and inferences.

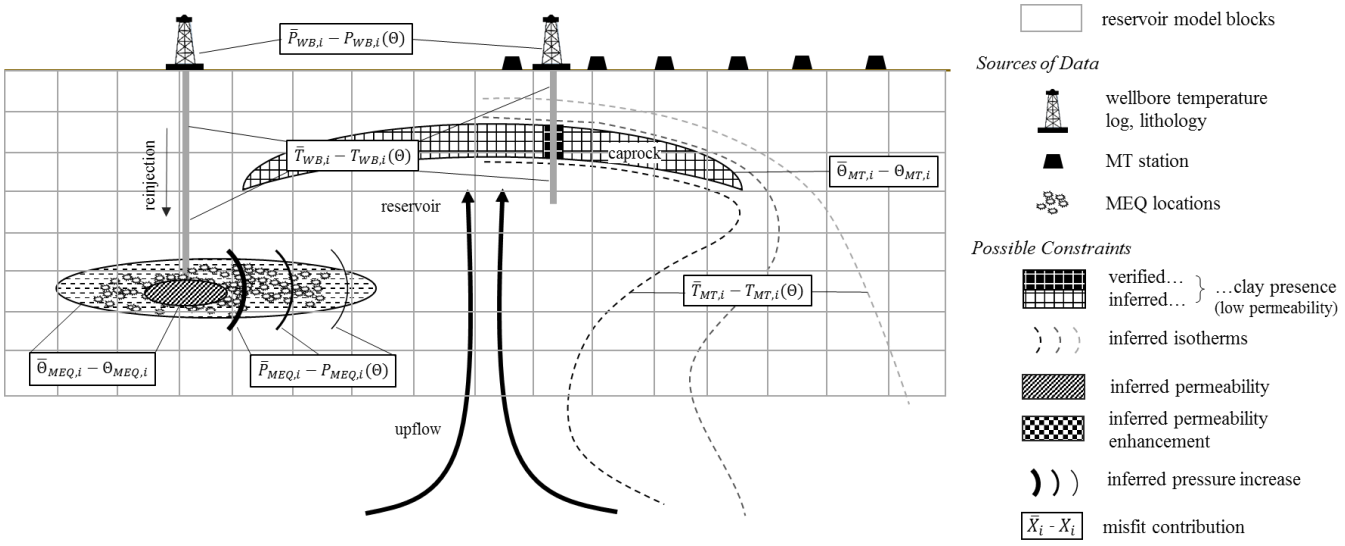

Figure 9: Schematic representation of MEQ (left of upflow) and MT integration (right of upflow) with the calibration of a reservoir model. Individual contributions to the misfit function are given in the enclosed boxes.

The main effect of including geophysical inferences in the misfit function will be to place constraint on the reservoir model in regions away from the borehole. Because the geophysical inversions are both constructed using wellbore data, they are unlikely to produce conflicting constraints in the areas where the geophysics and wells overlap.

5. CONCLUSION

In this paper, we have summarized recent efforts towards using geophysical datasets in the calibration of geothermal reservoir models. The main aim has been to incorporate physical relationships between reservoir quantities of interest – permeability, pressure, temperature – and quantities observed or inferred by remote sensing – electrical conductivity, MEQ location – into computational inversion frameworks. Specifically, we have demonstrated how, through the use of priors, wellbore information can be used as both hard and soft constraints on a pseudo-2D MT inversion. In utilizing an MCMC approach, our MT inversion also outputs intervals of uncertainty on the position of the clay cap. Furthermore, by linking the position of the clay cap to smectite formation temperature, we are able to estimate, with uncertainty, the approximate positions of isotherms distant from a well.

We have also outlined a methodology to interpret MEQ clouds in terms of local permeability changes and fluid pressure rise around an injection well. This builds on an earlier 1D radial inversion, but must compromise in the quantification of uncertainty so as to incorporate a larger number of free parameters. In any case, the results appear to confirm an earlier finding that MEQ clouds are often orders of magnitude larger than the volume of stimulated reservoir. If this is a general result, it has severe implications for the viability of EGS.

Aside from incremental improvements to the efficiency and accuracy of our inversion methods, the next obvious step is the application of these techniques in calibrating a real geothermal reservoir model. This presents several challenges, including the typically long runtime of natural state and production history models (hours to days), as well as finding a suitably well-characterized geothermal field for validation.

REFERENCES

Ardid, A., Dempsey, D., Bertrand, T., and Archer, R.: Uncertain Estimation of Subsurface Temperature Away from the Borehole Using Magnetotelluric Inversions, *Proceedings*, 40th New Zealand Geothermal Workshop, Taupo, New Zealand (2018).

Benato, S., Hickman, S., Davatzes, N. C., Taron, J., Spielman, P., Elsworth, D., Majer, E. L., and Boyle, K.: Conceptual model and numerical analysis of the Desert Peak EGS project: Reservoir response to the shallow medium flow-rate hydraulic stimulation phase, *Geothermics*, **63**, (2016), 139-156.

Bredehoeft, J. D., and Papadopulos, I. S.: Rate of Vertical Groundwater Movement Estimated from the Earth's Thermal Profile, *Water Resources Research*, **1**, (1965), 325-328.

Brodsky, E. E., and Lajoie, L. J.: Anthropogenic Seismicity Rates and Operational Parameters at the Salton Sea Geothermal Field, *Science*, **341**, (2013), 543-546.

Browne, P. R. L.: Hydrothermal alteration in active geothermal fields, *Annual Review Earth and Planetary Sciences*, **6**, (1978), 229–250.

Dempsey, D., Suckale, J., and Huang, Y.: Collective properties of injection-induced earthquake sequences: 2. Spatiotemporal evolution and magnitude frequency distributions, *Journal of Geophysical Research*, **121**, (2016a), 10.1002/2015JB012551.

Dempsey, D., O'Sullivan, J., and Pearson, S.: Joint Inversion of Temperatures in a Synthetic Geothermal Field using MT, Clay Alteration Models, and Geothermal Reservoir Simulation, *Proceedings*, 38th New Zealand Geothermal Workshop, Rotorua, New Zealand (2016b).

Dempsey, D., Barton, C., and Catalinac, C.: Density of induced earthquake hypocenters as a proxy for pore pressure increase during well stimulation, *Proceedings*, 50th US Rock Mechanics/Geomechanics Symposium, Houston, Texas (2016c).

Grim, R. E.: Clay Mineralogy, 3rd Edition. McGraw-Hill, New York, (1968).

Gunderson, R., Cumming, W., Astra, U., and Harvey, C.: Analysis of smectite clays in geothermal drill cuttings by the methylene blue method: for well site geothermometry and resistivity sounding correlation. *Proceedings*, World Geothermal Congress, Kyushu-Tohoku, Japan, (2000), 1175–1181.

Mellors, R. J., Ramirez, A., Tompson, A., Chen, M., Yang, X., Dyer, K., Wagoner, J., Foxall, W., and Trainor-Guitton, W.: Stochastic Joint Inversion of a Geothermal Prospect, *Proceedings*, 38th Workshop on Geothermal Reservoir Engineering, Stanford University, Stanford, CA (2013).

Mellors, R. J., Tompson, A., Yang, X., Chen, M., Ramirez, A., and Wagoner, J.: Stochastic Joint Inversion Modeling Algorithm of Geothermal Prospects, *Proceedings*, 40th Workshop on Geothermal Reservoir Engineering, Stanford University, Stanford, CA (2015).

Milicich, S. D., Alcaraz, S., and Pearson-Grant, S. C.: An Integrated Approach to Geological and Fluid Flow Modelling: From a 3D Geological Model to TOUGH2, *Proceedings*, 37th New Zealand Geothermal Workshop, Taupo, New Zealand (2015).

Morrison, K.: Important hydrothermal minerals and their significance, *Geothermal and Mineral Service Div., Kingston Morrison Ltd*. (1997).

Murray, H.H.: Clays. Ullmann's Encyclopedia of Industrial Chemistry, 6th Edition. Wiley-VCH Verlag GmBH, Weinheim, Germany, (2000).

Peaceman, D. W.: Interpretation of well-block pressures in numerical reservoir simulation, *Society of Petroleum Engineering Journal*, **18**, (1978), 183-194.

Riffault, J., Dempsey, D., Karra, S., and Archer, R.: Microseismicity Cloud Can Be Substantially Larger Than the Associated Stimulated Fracture Volume: The Case of the Paralana Enhanced Geothermal System, *Journal of Geophysical Research*, **123**, (2018), 10.1029/2017JB015299.

Rivera, J. M., and Dempsey, D.: Forward and Inverse Modelling of Geothermal Microseismicity Using TOUGH2 Coupled With and Earthquake Simulator, *Proceedings*, 39th New Zealand Geothermal Workshop, Auckland, New Zealand (2017).

Shapiro, S. A., Huenges, E., and Borm, G.: Estimating the crust permeability from fluid-injection-induced seismic emission at the KTB site, *Geophysical Journal International*, **131**, (1997), F15–F18.

Segall, P., and Lu, S.: Injection-induced seismicity: Poroelastic and earthquake nucleation effects, *Journal of Geophysical Research*, **120**, (2015), 10.1002/2015JB012060.

Sewell, S. M., Cumming, W., Bardsley, C. J., Winick, J., Quinao, J., Wallis, I. C., Sherburn, S., Bourguignon, S., and Bannister, S.: Interpretation of Microearthquakes at the Rotokawa Geothermal Field, 2008 to 2012, *Proceedings*, 35th New Zealand Geothermal Workshop, Rotorua, New Zealand (2013).

Zyvoloski, G.: FEHM: A Control Volume Finite Element Code for Simulating Subsurface Multi-phase Multi-fluid Heat and Mass Transfer, Los Alamos, Los Alamos National Laboratory, (2007).